



Two types of Tibetan Plateau vortex genesis in June and the associated mechanisms

Yiqiong Tang¹ · Guoxiong Wu^{2,3} · Bian He² · Yimin Liu^{2,3,4} · Jiangyu Mao² · Tingting Ma²

Received: 8 October 2022 / Accepted: 23 April 2023
© The Author(s) 2023

Abstract

The Tibetan Plateau vortex (TPV) is a key system triggering rainfall over the Tibetan Plateau (TP) during the boreal summer. The TPV genesis mechanisms are complicated and its classification is a great challenge. This study attempts to elucidate these aspects. By introducing the standardized index of 24-h increment of equivalent potential temperature $\Delta_{24h}\theta_e$ at 500 hPa, all the TPV cases generated in June between 1980 and 2016 are classified as either positive or negative. Composite analysis is subsequently applied to the extremes of these two types, i.e., the first and last fifth-percentile cases with extremely negative and positive standardized $\Delta_{24h}\theta_e$, respectively. Results indicate that 70% of them occur in relatively warmer and wetter environments, with diabatic heating dominating the positive type and the dynamic effect of large-scale circulation dominating the negative type. For the extremely positive cluster, the geopotential-height increment over the TP exhibits a negative/west–positive/east dipole, which enhances the southerly flow over the western TP, while forming surface water–vapor convergence. Consequently, strong condensation heating occurs near the sub-cloud level, resulting in the development of potential vorticity below and eventually TPV genesis. For the negative cluster, local shear lines at 500 hPa and upstream troughs at 250 hPa occur at the TPV genesis location. In conjunction with anomalous westerlies, positive potential vorticity is generated in situ due to zonal advection. The retardation caused by the Kunlun Mountains on the impinging westerly flow associated with side-boundary friction also contributes to TPV genesis southeast of the mountains.

Keywords Tibetan Plateau vortex (TPV) · 24-h increment of equivalent potential temperature ($\Delta_{24h}\theta_e$) · Genesis mechanism · Potential vorticity (PV) budget

1 Introduction

Tibetan Plateau vortices (TPVs) are officially described as low-pressure cyclones with closed geopotential contours or cyclonic winds captured by at least three nearby stations at 500 hPa over the Tibetan Plateau (TP) (Lhasa Workgroup for Tibetan Plateau Meteorology Research 1981). Typically, TPVs are characterized as shallow systems with α -scales of 400–800 km in the horizontal direction and 2–3 km in the vertical direction (Ye and Gao 1979; Lhasa Workgroup for Tibetan Plateau Meteorology Research 1981; Feng et al. 2014; Curio et al. 2019; Lin et al. 2020). As a specific system over the TP, a TPV generally acts as a shallow system with vorticity maximum and a warm center at 500 hPa. TPVs are key systems triggering rainfall over the Tibetan Plateau (TP) during the boreal summer. TPV-associated precipitation accounts for more than 50% of the total precipitation over the TP during the warm season (Lin et al. 2021). Certain conditions may drive a few TPVs eastward from the

✉ Guoxiong Wu
gxwu@lasg.iap.ac.cn

✉ Bian He
heb@lasg.iap.ac.cn

¹ School of Atmospheric Sciences and Remote Sensing, Wuxi University, Wuxi 214105, China

² State Key Laboratory of Numerical Modelling for Atmospheric Sciences and Geophysical Fluid Dynamics (LASG), Institute of Atmospheric Physics, Chinese Academy of Sciences, Beijing 100029, China

³ University of Chinese Academy of Sciences, Beijing 100049, China

⁴ Chinese Academy of Sciences Centre for Excellence in Tibetan Plateau Earth Sciences, Beijing 100101, China

TP (Lin et al. 2020). TPVs moving off the TP may result in severe downstream natural disasters by inducing anomalous cyclonic circulation and ascending motion (Li et al. 2020a, b; Zhao et al. 2021; Fu et al. 2022).

Previous studies have focused on the physical processes associated with TPV genesis from both the dynamic and thermodynamic perspectives. Qian et al. (1984) identified six elements contributing to TPV genesis, including the combined effects of diabatic heating, stability, topography, friction in the boundary layer, and large-scale circulation, which can be summarized as dynamic and thermodynamic factors. The robust diurnal variation in atmospheric circulation over high-elevation areas contributes to a higher TPV genesis rate at night (Li et al. 2014a, 2018; Curio et al. 2019; Lin et al. 2020; Ma et al. 2020, 2022; Zhang et al. 2021). Regarding favorable large-scale circulation patterns, TPV genesis results from the divergence at 200 hPa between the westerly jets and the South Asia High (SAH), as well as the convergence at 500 hPa associated with northwesterlies from the westerly flow and southerlies from the monsoon trough over the Bay of Bengal (Feng et al. 2014; Li et al. 2014b; Li and Zhang 2021). In addition, southwesterly flow convergence over the western TP, where the surface is warm, is also favorable for TPV genesis, owing to slantwise vorticity development (Wu et al. 2022).

The impacts of regional forcing on TPV genesis have also been highlighted, particularly with regard to local surface sensible heating. From the perspective of energy conversion, Luo et al. (1991) and Luo and Yang (1992) found through case studies that TPV genesis is promoted by effective eddy potential energy owing to the inhomogeneity of surface sensible heating, while Shen et al. (1986) emphasized the impact of surface sensible heating on local TPV intensification combined with topography and proper synoptic process. Numerous studies have also addressed the effect of condensational latent heat on TPV genesis and development. As a trigger for instability in plateau environments, latent heat is essential for the TPV development (Wang 1987). Li et al. (2011) revealed the dominance of latent heating during a case of TPV genesis by comparing the vertical profile of the apparent heat source and the apparent moisture sink. Ma et al. (2020) and Wu et al. (2022) highlighted the PV generation due to the vertical inhomogeneity of diabatic heating associated with the wet process from the perspective of the PV budget. Results from numerical experiments (Tian et al. 2015; Wu et al. 2018; Zhang et al. 2019; Deng et al. 2022) indicated that the roles of different processes involving sensible and latent heating are case-independent.

The consensus is that TPV genesis occurs due to a combination of dynamic and thermodynamic factors; however, the relative contributions of the dynamic and thermodynamic

processes vary depending on the specific circumstances, and the characteristic delineation of the TPV classification based on the genesis mechanism is unclear. Currently, this topic is hampered by the lack of detailed and systematic analyses. Achieving consensus regarding the physical processes behind TPV genesis is challenging. In this study, we examine the mechanisms of TPV genesis in the June-mean climate based on reanalysis and TPV datasets. The selection of June TPVs for investigation was based on the following two considerations: First, since the atmospheric circulation over Asia shifts abruptly in early June and October (Ye et al. 1958), climate in June may exhibit summer characteristics. Second, TPVs occur frequently during the boreal summer, especially in June (Lin et al. 2020). By classifying June TPV generation, we provide a primary characteristic delineation of the TPV genesis mechanisms for different types of TPVs.

The remainder of this paper is organized as follows: In Sect. 2, we describe the datasets and methodology used in this study. In Sect. 3, we present the characteristics of the June-mean TPV distribution and key index of the 24-h increment of surface equivalent potential temperature $\Delta_{24h}\theta_e$, based on which we identify two extreme types of TPV genesis background, i.e., warm and moist versus cold and dry conditions. In Sects. 4 and 5, we present detailed mechanistic analyses of these two types of TPV genesis. In Sect. 6, we discuss the findings and present the conclusions.

2 Data and method

2.1 Dataset

TPVs are identified primarily manually (i.e., subjectively) using historical weather maps and observations (Wang et al. 2009) or automatically (i.e., objectively) using reanalysis data (Lin et al. 2013, 2020). The automatic objective TPV identification is reproducible and consistent, contrary to the manual method. The TPV database used in this study was obtained by Lin et al. (2020) through objective identification using reanalysis data. The authors confirmed through validation among multiple reanalysis datasets that the MERRA-2 and ERAI datasets have the highest matching rate; additionally, the MERRA-2 dataset is more precise. Moreover, it has been demonstrated that the MERRA-2 dataset is trustworthy for identifying TPVs and delineating the circulation over the TP (Lin et al. 2020; Ma et al. 2020). Thus, the TPV database chosen for this study is the one identified objectively based on the MERRA-2 dataset.

The 1980–2016 MERRA-2 reanalysis dataset was adapted for circulation and thermal analysis with a horizontal resolution of $0.5^\circ \times 0.625^\circ$ at 42 isobaric levels (Gelaro et al. 2017), involving meteorological elements, such as horizontal wind, vertical velocity, air temperature, pressure, specific humidity, and diabatic heating rate and its components.

2.2 Methodology

2.2.1 24-h increment of equivalent potential temperature index $\Delta_{24h}\theta_e$

The equivalent potential temperature is given by $\theta_e = \theta \cdot \exp\left(\frac{Lq}{C_p T}\right)$, where θ is the potential temperature, L is the latent heat of condensation, and q is the specific humidity; it is a useful tool for comparing air temperature and moisture content, and is used operationally to map unstable areas (Chen et al. 2017). In this study, we calculate θ_e at the TPV genesis time as well as 24 h before that, and define the difference between the two as the index $\Delta_{24h}\theta_e$, i.e., the 24-h increment of equivalent potential temperature. For the definition of TPV and the consistency of subsequent analysis, $\Delta_{24h}\theta_e$ at 500 hPa is utilized in the study.

2.2.2 PV budget equation

The PV budget diagnosis considers both dynamic and thermodynamic factors; hence, it can be an effective tool for understanding the TPV genesis (Li et al. 2011; Wu et al. 2018, 2022; Ma et al. 2020). The celebrated PV equation in isobaric coordinates is the following (Ertel 1942; Hoskins et al. 1985; Wu et al. 2022):

$$\frac{\partial PV}{\partial t} = -\vec{V}_h \cdot \nabla_h PV - \omega \frac{\partial PV}{\partial p} - g \vec{\zeta}_{ap} \cdot \nabla_p \dot{\theta} - g(\nabla_p \times \vec{F}) \cdot \nabla_p \theta, \quad (1)$$

where $\vec{\zeta}_{ap}$ is the absolute vorticity, $\dot{\theta} = \frac{d\theta}{dt}$ denotes the diabatic heating, and $PV = -g \vec{\zeta}_{ap} \cdot \nabla_p \theta$ denotes the Ertel PV. Other variables are conventional in meteorology. In Eq. (1), the left-hand side is the local PV change and the terms on the right-hand side are the vorticity advection divided into horizontal and vertical parts, diabatic heating, and friction, respectively. In the following, we employ Eq. (1) to identify the distinct contributions of various terms to PV generation in different types of TPV genesis.

2.2.3 Water–vapor flux and its divergence

Water–vapor transport and latent heating are involved in the genesis of certain TPVs (Li et al. 2011; Ma et al. 2022; Wu et al. 2022). To examine whether they are involved in the genesis of all TPVs, we calculate the water–vapor flux and the associated divergence for different types of TPV genesis using the following formula (Wu et al. 2022):

$$\begin{cases} Q = \frac{q \vec{V}_h}{g} \\ D = \frac{1}{g} \nabla \cdot (q \vec{V}_h) \end{cases}, \quad (2)$$

where \vec{V}_h is the horizontal wind vector.

Additionally, we used mathematical statistical analysis methods, including probability density function, TS-test and composite analysis.

3 TPV genesis classification based on the $\Delta_{24h}\theta_e$ index

Wu et al. (2022) revealed with a case study that a positive increase in the 24-h equivalent potential temperature (i.e., $\Delta_{24h}\theta_e > 0$) is a noteworthy indicator of TPV genesis over the western TP. A time span of 24 h was chosen to eliminate the impact of the diurnal cycle. High sub-cloud entropy associated with large positive $\Delta_{24h}\theta_e$ during TPV genesis not only suggests the pooling of warm and moist air, but also favors convective development since the large-scale circulation in a convective atmosphere is closely related to the spatiotemporal distribution of sub-cloud entropy (Emanuel et al. 1994). Therefore, we selected the $\Delta_{24h}\theta_e$ index as a TPV-genesis classification criterion and we shall henceforth dub it X index.

3.1 Spatial characteristics of TPV genesis based on the $\Delta_{24h}\theta_e$ index

A total of 374 June TPVs were generated between 1980 and 2016. The locations of the June TPV genesis and the spatial distribution of the corresponding $\Delta_{24h}\theta_e$ index (X) during 1980–2016 are presented in Fig. 1. Numerous TPVs originate from the western TP, particularly the mountainous area (35° N, 78°–90° E; elevation: ~5500 m) (Fig. 1a); conversely, June TPVs over the eastern TP are scattered. Almost 70% of the TPV generates where characterized by a positive $\Delta_{24h}\theta_e$ index, with the magnitude of the most positive $\Delta_{24h}\theta_e$ index value exceeding that of the most negative $\Delta_{24h}\theta_e$ index value by a factor of two. We note that although only a few extremely positive/negative X -index cases occurred over the eastern TP, with the mean value of $\Delta_{24h}\theta_e$ index over the eastern TP being 2.92 K, i.e., much larger than the mean value of $\Delta_{24h}\theta_e$ index 1.72 K over the western TP (the eastern–western TP is bounded by 90° E). This is because as a function of temperature and specific humidity, $\Delta_{24h}\theta_e$ over the warmer and moister eastern TP is much higher than that over the colder and drier western TP. For fair evaluation, the original index sequence $X(i) = X(i = 1, 2, \dots, M = 374)$ was standardized, respectively, over the western and eastern TP using the following formula:

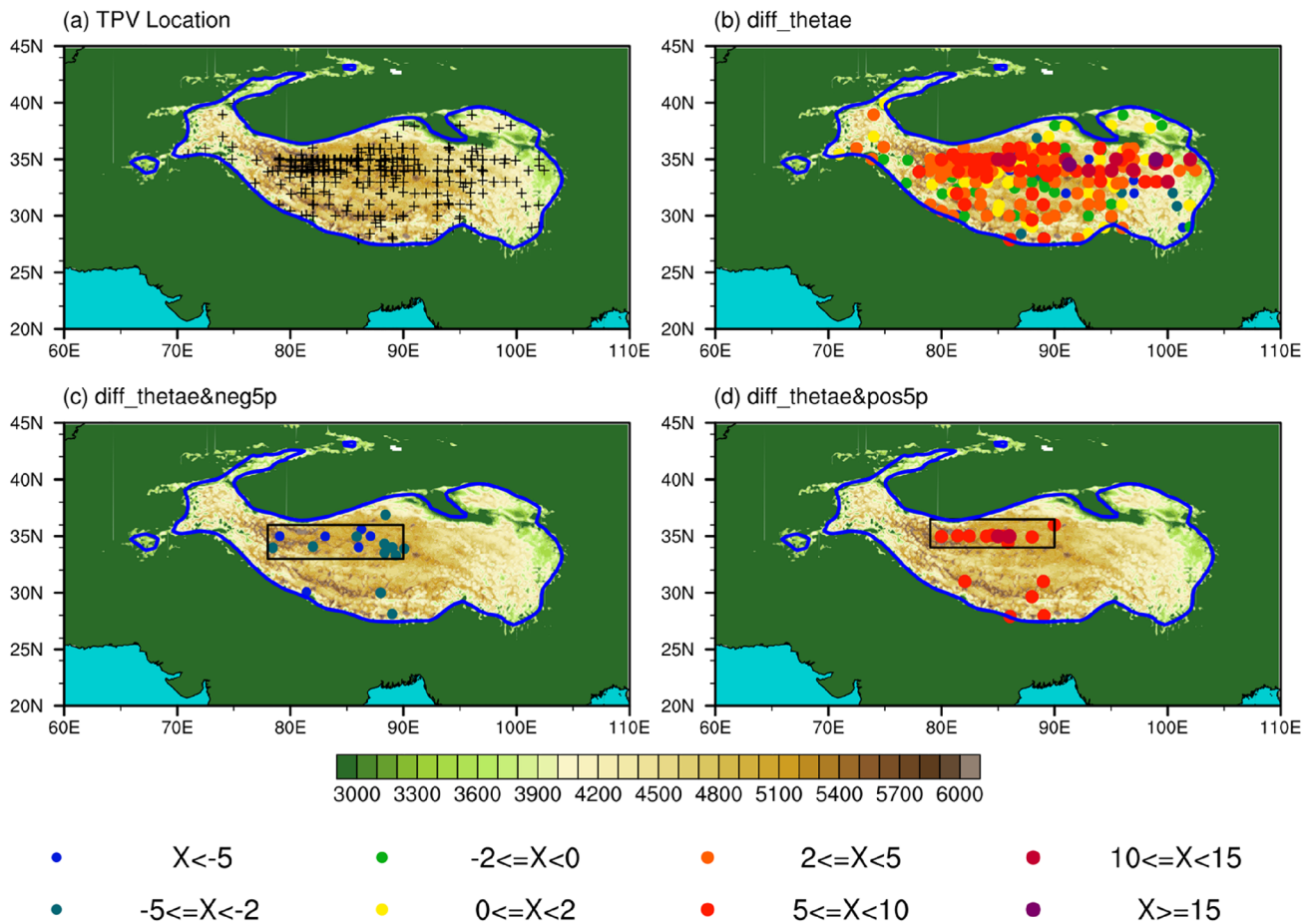


Fig. 1 **a** Genesis locations (black crosses) of June TPVs during 1980–2016, **b** the corresponding original $\Delta_{24h}\theta_e$ (i.e., X), index values (colored dots; unit: K), and genesis locations of the June TPVs with the 5% extreme most **c** negative and **d** positive standardized $\Delta_{24h}\theta_e$ (i.e., Y) index values. The background color indicates the elevation

(unit: m). The areas in the black boxes (i.e., 33°–36° N, 78°–90° E and 34.0°–36.5° N, 79–90° E in panels **c**, **d**, respectively) indicate the two key regions of high TPV occurrence. The solid blue contour lines in all panels indicate the TP boundary at 3000 m

$$\left\{ \begin{array}{l} Y(i) = \frac{X(i) - \bar{X}}{S_X} \\ \bar{X} = \frac{1}{N} \sum_{i=1}^N X(i) \\ S_X = \sqrt{\frac{\sum_{i=1}^N [X(i) - \bar{X}]^2}{N}} \end{array} \right. , \quad (3)$$

where $X(i)$ is the initial sequence $X (i = 1, 2, \dots, M = 374)$ of the X (i.e., $\Delta_{24h}\theta_e$) index for both parts of the TP, \bar{X} is the area-mean of the initial sequence which is 2.92 K for the eastern TP and 1.72 K for the western TP, N is the number of the TPV cases in the corresponding area, S_X is the corresponding standard deviation, and $Y(i)$ is the corresponding standardized $X(i)$ index. Then the two standardized sequences from the eastern and western TP are rejoined as

the standardized index Y . In the following, percentile analysis is applied to the rejoined time series of $Y(i)$ to reveal the distinct features of different types of TPV genesis.

3.2 Standardization index and selected cases

The probability density function distribution of the $\Delta_{24h}\theta_e$ index before and after standardization is shown in Fig. 2. The standardized $\Delta_{24h}\theta_e$ index, i.e., Y satisfies a normal distribution with a mean of 0 and a standard deviation of 0.287. Y values range from 0 to 1. And it passes a KS-test with a significance of 0.001 which is a non-parametric test for goodness of fit. Before standardization, the percentage of positive X -index cases is twice as high as that of the negative X -index cases. After standardization, the two types are evenly distributed with comparable magnitudes. We note that all the extreme cases within the first (i.e., < 5%) and last (i.e., > 95%) fifth percentiles occur over the western TP over

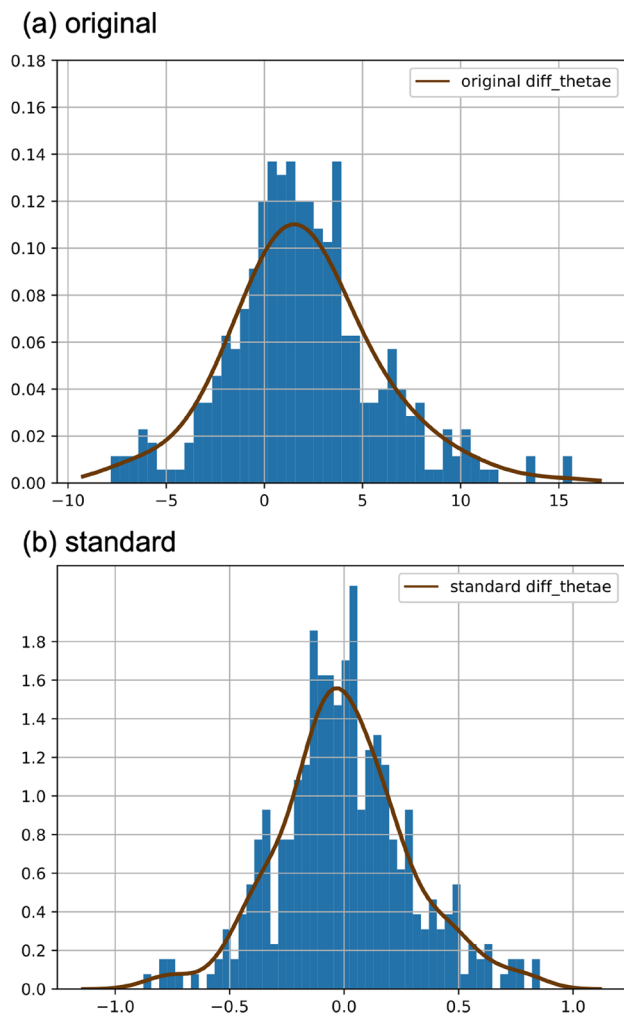


Fig. 2 Histograms and fitted probability density functions of the index at the TPVs genesis time in June during 1980–2016 **a** before and **b** after standardization. The horizontal coordinate in panel **a** is the original $\Delta_{24h}\theta_e$ (i.e., X) index (unit: K) and the one in panel **b** is the standardized $\Delta_{24h}\theta_e$ (i.e., Y) index. The vertical coordinates in both panels are the probability density functions (PDFs)

the two key regions 33° – 36° N, 78° – 90° E and 34.0° – 36.5° N, 79° – 90° E, as shown in Fig. 1c, d, respectively. The first and last fifth-percentiles are used as thresholds for selecting samples from the standardized sequences for composite analysis. Overall, 19 extremely negative and positive Y -index cases were selected for the negative and positive composite analyses, respectively.

The equivalent potential temperature (i.e., θ_e) is a variable dependent on both the temperature and humidity conditions. Figure 3 shows the distributions of the 24-h increments of potential temperature and specific humidity at 500 hPa for the selected positive and negative cases. During TPV genesis, when θ_e increases significantly (Fig. 3a), pronounced increases in both potential temperature and specific humidity occur over the central and western TP, where the region

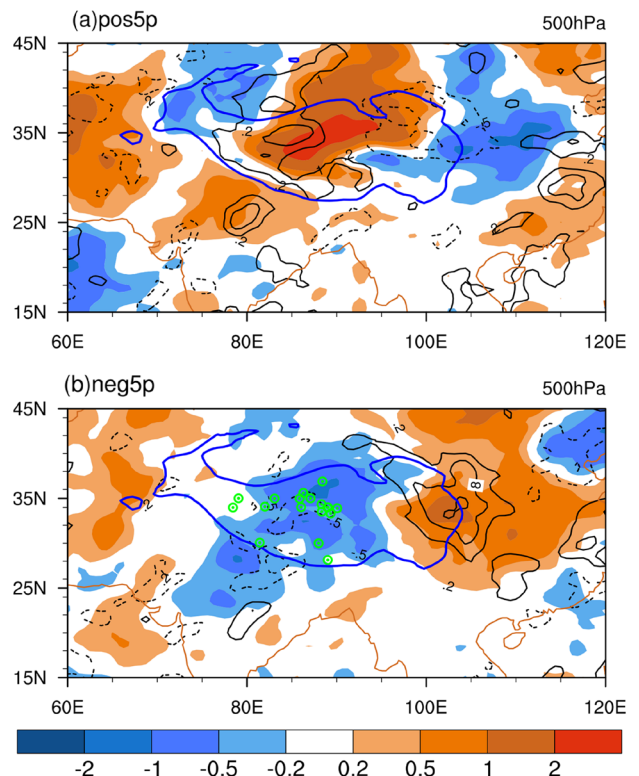


Fig. 3 The 24-h increments of potential temperature (shading; unit: K) and specific humidity (contours, with solid and dashed lines denoting positive and negative values, respectively; unit: 10^{-5} kg kg^{-1}) at 500 hPa for the 5% extreme **a** positive and **b** negative index cases. Green dots in panel **b** denote the genesis locations of the 19 negative index cases. The solid blue contour lines in both panels indicate the TP boundary at 3000 m

favoring TPV genesis is situated (Fig. 1a); conversely, when θ_e decreases significantly (Fig. 3b), the TPVs are generated in colder and drier environments. Usually, a warm surface corresponds to air convergence; thus, enhanced southerlies at 500 hPa develop at different locations over the TP involving different θ_e changes (Fig. 4): For positive cases, southerlies develop over the central TP (Fig. 4a); for negative cases, southerlies develop over the eastern edge of the TP (Fig. 4b). Such circulation changes result in different mechanisms of TPV genesis, which we discuss in detail in the following two sections.

4 Circulation and heating features of the two extreme types

Wu et al. (2022) demonstrated with a case study that a positive $\Delta_{24h}\theta_e$ corresponds to increasing water vapor transport owing to a specific anomalous circulation pattern and to the concurrent enhanced latent heat release associated with moist processes; these are favorable diabatic conditions for

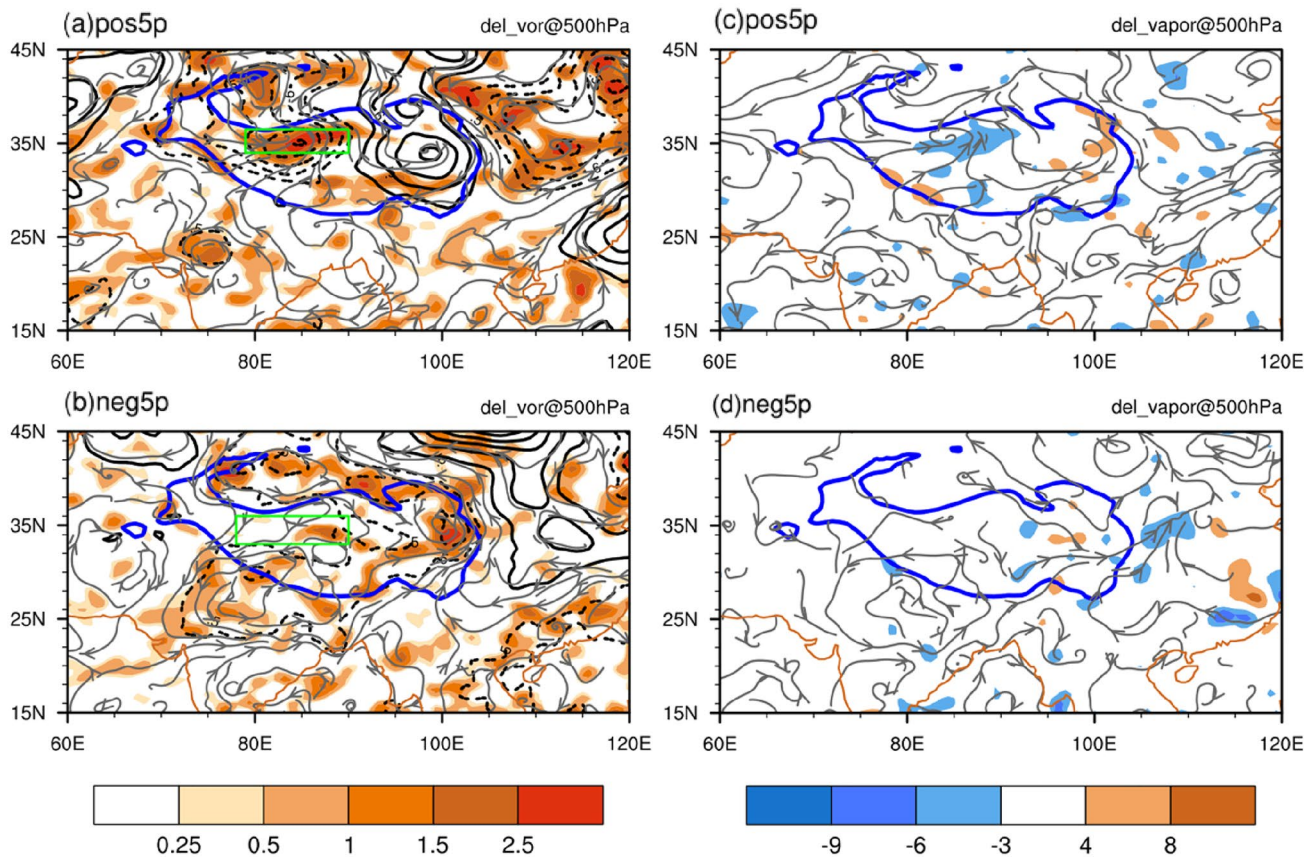


Fig. 4 Distributions at 500 hPa of the 24-h increments of **a, b** vorticity (shading; unit: 10^{-5} s^{-1}), geopotential height (contours, with solid and dashed lines denoting positive and negative values, respectively; interval: 3 gpm), and streamlines, and **c, d** divergence of water vapor flux (shading; unit: $10^{-6} \text{ g s}^{-1} \text{ kg}^{-1}$) and water vapor flux. Panels **a,**

c depict the 5% most positive index cases, and panels **b, d** depict the 5% most negative index cases. The green boxes in panels **a, b** correspond to the key areas shown in Fig. 1c, d, respectively. The solid blue contour lines in all panels indicate the TP boundary at 3000 m

TPV development. In this study, we employed the June-mean climate data to examine these conditions from the perspective of the anomalous circulation pattern, water vapor transport, vertical motion, and vertical inhomogeneity of diabatic heating.

4.1 Anomalous circulation and water vapor transport

The distributions of the 24-h increments of vorticity, geopotential height, and water vapor transport at 500 hPa are shown in Fig. 4. For the extremely positive index cases (Fig. 4a), vorticity growth develops over the western TP, where most June TPVs originate from (Fig. 1a), while negative vorticity growth develops over the eastern TP. Correspondingly, an obvious dipole mode of the 24 h-increment of geopotential height is evident over the TP, exhibiting a “negative over the west and positive over the east” distribution. Owing to the dipole mode of the 24 h-increment of geopotential height, a prominent 24 h-increment southerly

flow directed from South Asia toward the TP’s interior prevails over the western TP (Fig. 4c); this southerly flow is coupled with the strong positive 24 h-increment of potential temperature, as shown in Fig. 3a. The enhanced southerlies cause not only water vapor transport (Fig. 4c), but also the formation of cyclonic circulation. In addition, the positive 24 h-increment of geopotential height over the northwestern Pacific, implies enhanced subtropical high. For the negative index cases (Fig. 4b), a prominent geopotential height trough is evident over the TP, and a remarkable geopotential height ridge is prevalent over eastern China. A zonally oriented anticyclonic circulation wedges into the northwestern TP and north of the cyclonic circulation over northern India. A narrow convergent zone is thus produced between the anticyclonic circulation in the north and the cyclonic circulation in the south, thereby forming a so-called “shear line” zone with weak positive 24 h-increment of vorticity. In accordance with the circulation variations, changes in the water vapor flux and its convergence also exhibit different distributions over the TP. For the positive 24 h-increment

type, a strong convergence center of water vapor flux appears over the northwestern TP (Fig. 4c); this is in accordance with the 24 h-increment of vorticity (Fig. 4a) and indicative of the important role of moist processes in TPV genesis. Conversely, for the negative 24 h-increment, there is no significant water vapor convergence over the TP (Fig. 4d), instead, a band of water vapor convergence appears to the east of the TP, having the prominent cyclone over the TP on its west and the anticyclonic circulation over eastern China on its east.

4.2 Associated ascend motion

TPVs genesis is closely related to atmospheric divergence in the upper layer and convergence in the lower layer (Li et al. 2014a, b; Li and Zhang 2021; Lin et al. 2021). To explore the vertical air motions related to different types of TPVs, the 24-h increments of vertical velocity and divergence averaged over the corresponding key regions, as shown in Fig. 1c, d, are shown in Fig. 5. For the positive index cases (Fig. 5a), the remarkable convergence at 500 hPa and divergence in the upper layers are both enhanced by approximately 10^{-5} s^{-1} within 24 h west of 92° E over the TP, thereby forming locally prominent air ascent. The relationship between large-scale circulation and TPV activity in the positive index cases is consistent with previous studies (Li et al. 2014a, b; Li and Zhang 2021; Lin et al. 2021). For the negative index cases (Fig. 5b), the scattered upper-level divergence and lower-level convergence are distributed east of 85° E , while the enhancement of divergence at the lower layer appears in the western TP.

4.3 Impact of diabatic heating

The thermal diurnal cycle over the TP is robust; it generally exhibits strong surface heating that decreases with increasing height during the day and strong surface radiative cooling during the night. Usually, surface PV generation during the night is balanced by surface PV dissipation during the day, thereby forming a typical thermal diurnal cycle. According to Wu et al. (2022), the TPV case in late June 2016 was generated when such a typical diurnal cycle was interrupted during the night by abnormal PV generation associated with latent heat release.

Figure 6 presents the vertical profiles of the 24-h increment of diabatic heating averaged over the two key regions during TPV genesis. For the positive index cases (Fig. 6a), heating near the surface during TPV genesis is weaker compared with that in the previous day. The maximum increase in diabatic heating (i.e., up to $4 \times 10^{-5} \text{ K s}^{-1}$) occurs at 400–350 hPa mainly due to moist processes. Following the PV Eq. (1),

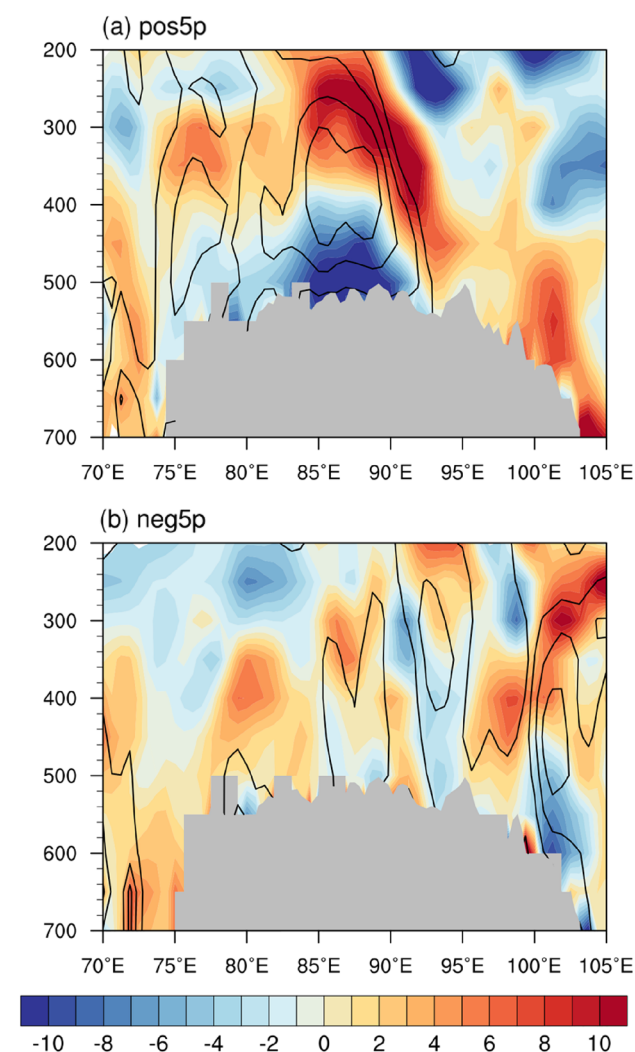


Fig. 5 Height–longitude cross-section of the 24-h increments of divergence (shading; unit: 10^{-6} s^{-1}) and vertical air ascent (contours; interval: 0.04 Pa s^{-1}) averaged **a** between 34° N and 36.5° N for the 5% extreme positive index cases and **b** between 33° N and 36° N for the 5% extreme negative index cases. Gray shading in both panels indicate surface pressure

$$\frac{\partial PV}{\partial t} \propto -g \vec{\zeta}_{ap} \frac{\partial \theta}{\partial p} \tag{4}$$

the rapid increase in diabatic heating with increasing height in the lower troposphere can result in PV generation near the surface, thereby favoring TPV genesis; it is a justifiable circulation and diabatic heating configuration leading to TPV genesis for positive index cases. For the negative index cases (Fig. 6b), heating near the surface during TPV genesis changes only slightly compared with that in the previous day, whereas the diabatic heating near 350 hPa declines remarkably, resulting in reduced PV generation; this suggests that, for negative index cases, diabatic heating is not a decisive aspect of TPV genesis.

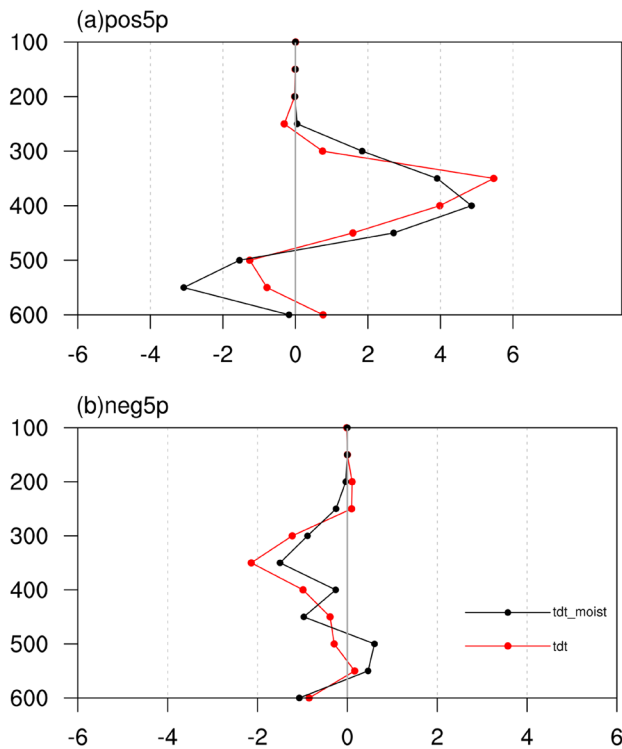


Fig. 6 Vertical profiles of the 24-h increments of diabatic heating (red solid line; unit: 10^{-5} K s^{-1}) and diabatic heating associated with moist processes (black solid line; unit: 10^{-5} K s^{-1}) for the 5% extreme **a** positive and **b** negative index cases averaged over the corresponding key regions

5 TPV genesis environment for extremely negative index cases

The above analyses demonstrated that approximately 70% of the TPVs in June are generated under warmer or wetter background conditions, in which diabatic heating plays a significant role. The physical processes are similar to those identified in a case study of TPV genesis in late June 2016 (Wu et al. 2022); however, the process that dominates TPV genesis under colder and drier background conditions (i.e., with a negative Y -index), remains unclear. To elucidate these aspects, we first employ a case study and subsequently a composite analysis.

5.1 Case study

We start with a negative index case that occurred on June 12, 2000; the case was selected because it occurred in a simultaneously extremely drier and colder environment (Fig. 3b). We note that a zonal shear line with positive vorticity was present during the day of June 11, 2000, i.e., before TPV genesis.

Figure 7 shows the evolution of the divergence of water vapor flux and 24-h increment of θ_e (Fig. 7a–c), as well as

the evolution of positive relative vorticity and streamlines (Fig. 7d–f) at 500 hPa. During the case development over the western TP, there was no significant water vapor convergence, and θ_e decreased markedly, with the $\Delta_{24h}\theta_e$ minimum reaching -8 K . A band of convergence of water vapor flux appeared over the eastern TP owing to another TPV genesis. The 24-h increment of θ and specific humidity were both extremely negative over the western TP (figures not shown), and the magnitudes of cooling and drying increased gradually before TPV genesis. The evolutions of relative vorticity and stream field before the TPV genesis (Fig. 7d–f) demonstrated that a zonally oriented “shear line” with increasing relative vorticity was present. The stream field presented a unique feature with an increasing cyclonic curvature along the shear line and an anticyclonic curvature to the north, while the TPV was generated at the eastern end of the shear line. This peculiar phenomenon will be studied further through composite analyses.

Next, we briefly analyze the circulation background of TPV genesis. The distributions of the large-scale circulation and zonal wind speed at 250 and 500 hPa on June 12, 2000, at 0000 local time (LT) are presented in Fig. 8, along with the mid-June climatology. In the climate mean at 250 hPa (Fig. 8a), westerly airflow prevails with PV being zonally distributed over the TP. The SAH on June 12, 2000 (Fig. 8b), was much stronger than that in the climatology, with a center of more than 11,050 gpm located just south of the TP and the salient trough–ridge system developed along the westerlies north of the TP. A strong deep trough with an intensity of more than 5 PVU, i.e., approximately triple that of the climate mean, invaded the northwestern TP. Consequently, anomalously low geopotential height and positive PV prevailed over the northwestern TP during the case genesis (Fig. 8b). At 500 hPa, the climate-mean westerly flow is prevalent in the mid-latitudes, with a zonal speed less than 5 m s^{-1} over the TP and a deep trough formed over the Bay of Bengal (Fig. 8c). On the night of June 12, 2000 (Fig. 8d), the anomalous trough–ridge system developed strongly north of the TP, and the geopotential height over the TP platform declined. Similar to the upper troposphere, a large trough extended southward over the Tarim-Jungar Basin, in association with the development of the upstream ridge. Consequently, anomalous positive vorticity developed over the northwestern TP in tandem with the in-situ shear line (Fig. 7f). At the bottom of the trough, i.e., just north of the TP, the zonal wind speed exceeded 17 m s^{-1} , being about triple that of the climate mean. In addition, the zonal wind speed along the shear line reached 11 m s^{-1} , being more than double that of the climate mean. Generally, the circulation pattern favors zonal positive PV advection over the northwestern TP and vorticity development along the existing shear line.

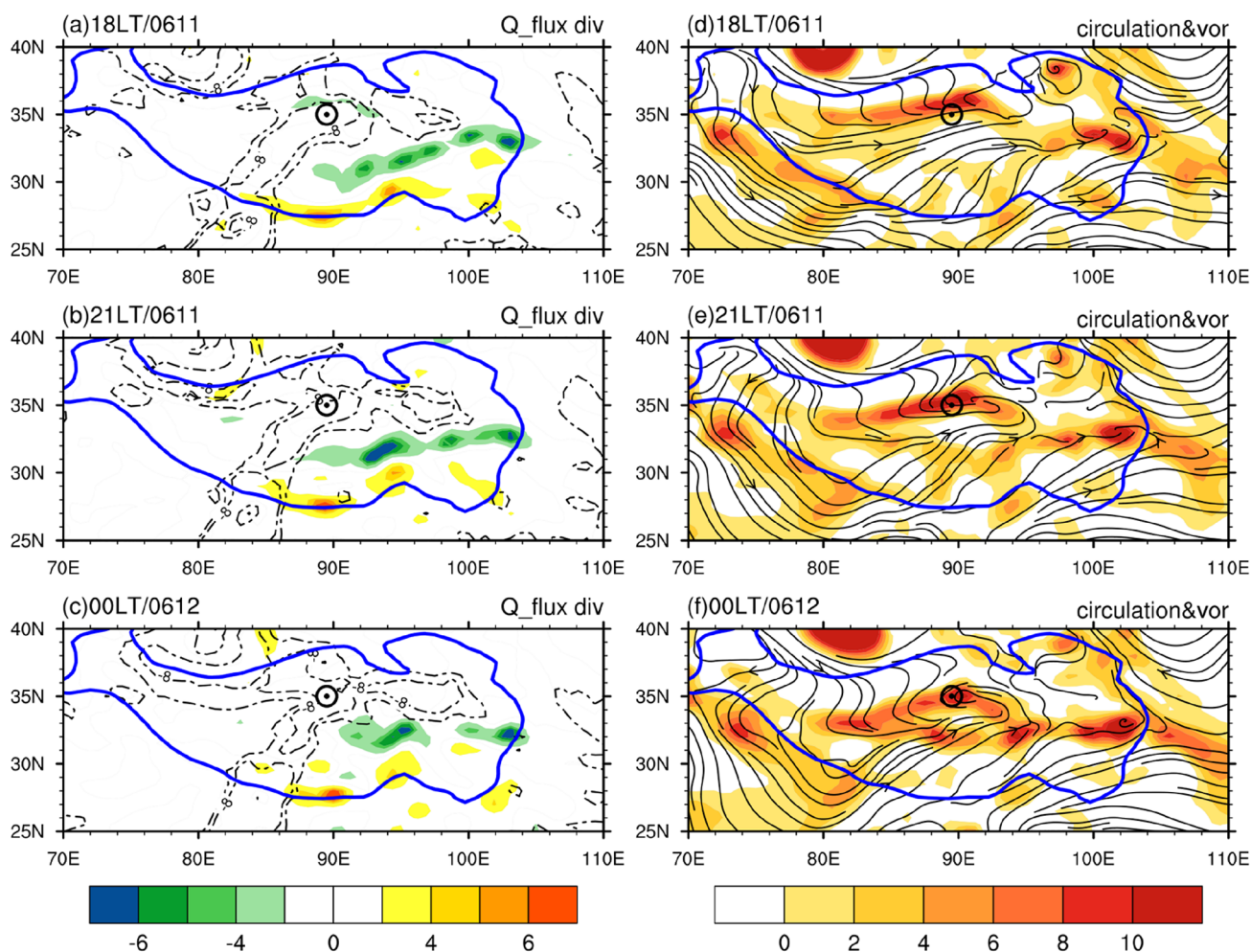


Fig. 7 Distributions at 500 hPa of **a–c** divergence of water vapor flux (shading; unit: $10^{-5} \text{ g s}^{-1} \text{ kg}^{-1}$) and 24-h increment of equivalent potential temperature (dashed contours, with only less than -4 K shown; unit: K), and **d–f** the corresponding vorticity (shading; unit: 10^{-5} s^{-1}). Streamlines in panels **a**, **d** correspond to June 11, 2000, at

1800 LT, in panels **b**, **e** correspond to June 11, 2000, at 2100 LT, and in panels **c**, **f** correspond to June 12, 2000, at 0000 LT. Black circles indicate the TPV genesis location. The solid blue contour lines in all panels indicate the TP boundary at 3000 m

To analyze the qualitative contributions of the dynamic and thermodynamic factors to the PV generation associated with this TPV genesis, we performed a PV-budget diagnosis for the TPV genesis location (Fig. 9). On June 11, 2000, at 1800 LT, there was a weak PV generation at the TPV genesis location, with the main source being the diabatic heating term, while the vorticity advection term had a weak negative contribution. During the night, the PV tendency increased markedly at 2100 LT as well as three hours later; the contribution of the PV advection term was more than twice as that of the diabatic heating term. In addition, both positive zonal and vertical PV advectons were favorable for TPV genesis. Zonal vorticity advection was closely associated with the significant development of zonal wind upstream and anomalous cyclonic circulation (Fig. 8). The positive contribution of the vertical PV advection arose from both the

ascending flow along the shear line and the increased surface PV associated with the increasing surface static stability at night (figure not shown).

5.2 Composite analysis of TPV genesis for the extremely negative index cases

To verify whether the above results obtained from the case study are representative of TPV genesis under colder and drier backgrounds, we conducted a composition analysis to investigate the dynamic impact on the genesis of the 19 TPVs with extremely negative index values within the first fifth percentile. Figure 10 shows the distributions of large-scale circulation, zonal wind speed, and geopotential height at 250 hPa in June. For the 1980–2016 climate mean, the SAH is located south of 25° N , while westerly flow prevails

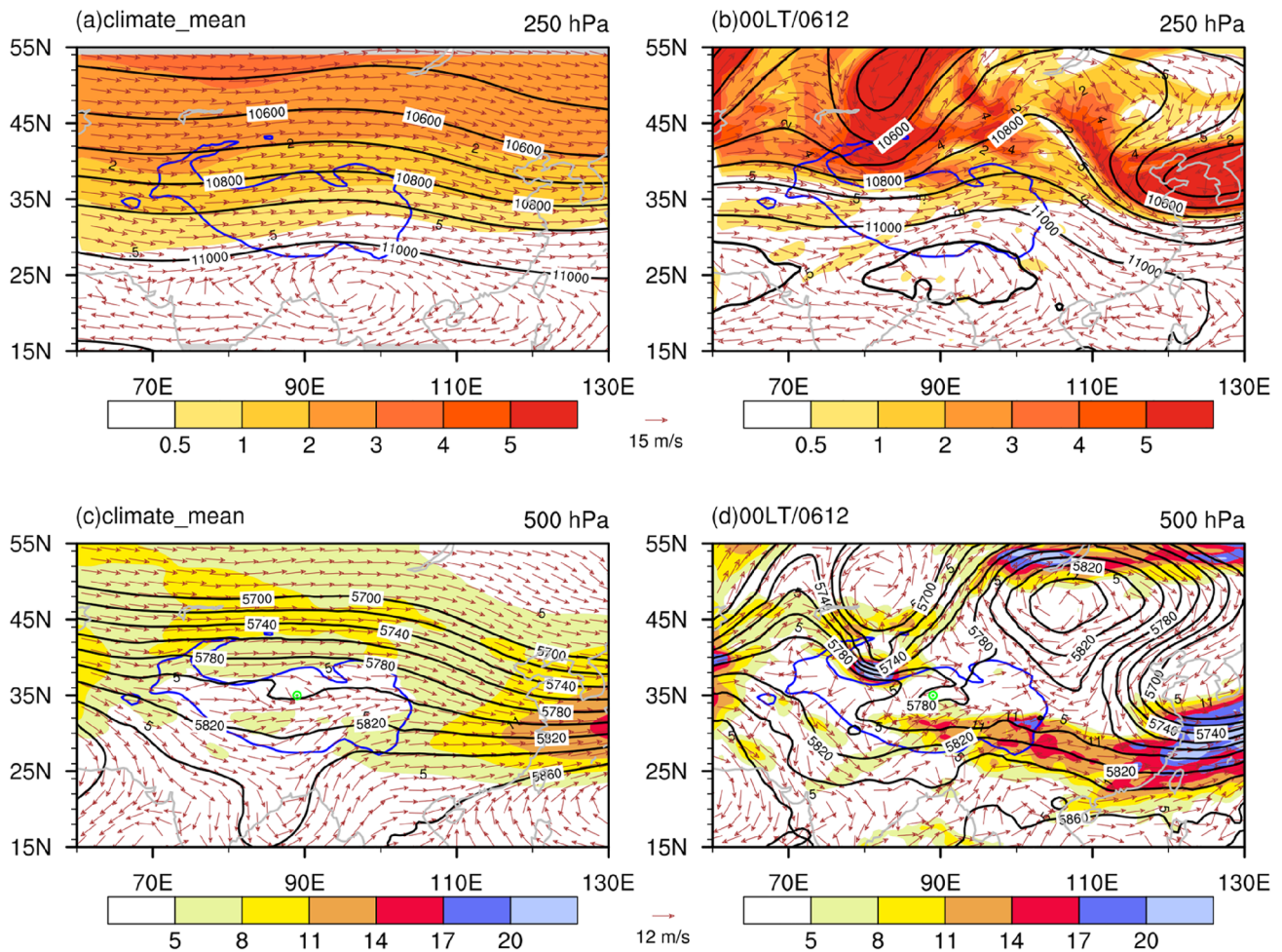


Fig. 8 Horizontal distributions of **a, b** geopotential height (contour; unit: gpm), wind field (vectors), and PV (shading; unit: PVU) at 250 hPa, and **c, d** geopotential height (contour; unit: gpm), wind field (vectors), and zonal wind speed (shading; unit: m s^{-1}) at 500 hPa.

Panels **a, c** show the mid-June climatology, and panels **b, d** show the conditions on June 12, 2000, at 0000 LT. The solid blue contour lines in all panels indicate the TP boundary at 3000 m

over the TP (Fig. 10a). For the composite of the extremely negative index cases, the center of the SAH moves north-eastward from over Bangladesh to the southeastern tip of the TP (Fig. 10b). Consequently, a decreased geopotential height anomaly occurs over the northwestern TP, whereas anomalous positive geopotential height develops from the southeastern TP to the western Pacific region (Fig. 10c). Therefore, the anomalous westerly flow prevails over the northwestern TP, thereby favoring the transport of positive PV from the trough to the TPV genesis region. The corresponding composite 24-h increment at the TPV genesis time also demonstrates decreasing geopotential height over the western TP and increased geopotential height over the east (Fig. 10d), thereby strengthening the westerlies over the southwestern TP and the easterlies over the northwestern TP.

Similar anomalies in geopotential height, zonal wind speed, and streamlines occurs at 500 hPa over the western

TP. As shown in Fig. 8c, in the climate mean, when the westerly flow encounters the TP, a weak ridge north of the TP and a large trough over the Bay of Bengal form concurrently, and the flow converges over the eastern TP. Anticyclonic circulation occupies the northwestern Pacific region. For the negative index cases (Fig. 11a), the subtropical high over the western Pacific and the westerly belt to the north are both shifted northward, thereby resulting in an anomalous easterly belt extending from the northwestern Pacific Ocean to the south of the TP. Furthermore, the anomalous subtropical circulation at 500 hPa is increased in the east and decreased in the west, with remarkable negative geopotential height anomalies over the entire TP (Fig. 11b). Anomalous westerlies develop over the western TP in the south and easterlies in the north, thereby forming a cyclonic shear line along 35°N , where the ridge of the Kunlun Mountains is located (Fig. 11c).

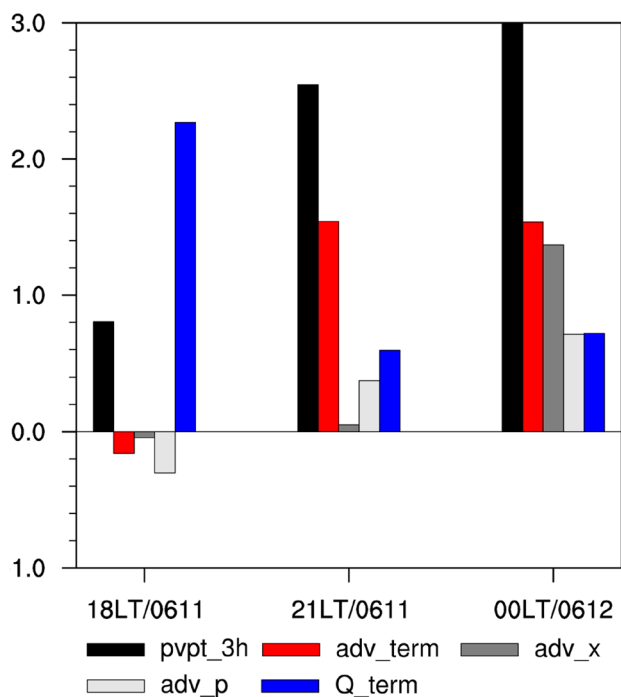


Fig. 9 Evolution of the 3-hourly PV tendency term (black bars), PV advection term (red bars), and its zonal (dark gray bars) and vertical (light gray bars) components, and diabatic heating term (blue bars) at the TPV location at 500 hPa during the night of June 11–12, 2000 (unit: $10^{-11} \text{ K m}^2 \text{ kg}^{-1} \text{ s}^{-2}$)

We note that the main part of the Kunlun Mountain Ranges is within the key region of the extremely negative type of TPV genesis, with its zonally oriented ridgeline penetrating the whole key region. Anomalous anticyclonic circulation accompanied by negative relative vorticity develops north of the mountain ridge, whereas anomalous cyclonic circulation accompanied by positive relative vorticity develops south of the mountain ridge (Fig. 11c). Such a circulation distribution is reminiscent of the analytical study of Thorpe et al. (1993) regarding the friction impact of a zonally oriented and isolated mountain on circulation: When westerly flow travels around such a mountain, the surface friction of the mountain retards the westerly flow more seriously close to the surface than at distance; negative relative vorticity generation is induced north of the mountain by friction, while positive relative vorticity generation is induced south of the mountain. Thorpe et al. (1993) also demonstrated that with westerly flow advection, subsequent anticyclone circulation is generated at the northeastern end of the mountain, whereas cyclone circulation is generated at its southeastern end. This is indeed the case in the extremely negative type of TPV genesis, characterized by prevailing westerly flow over the Kunlun Mountains (Fig. 11a). As shown in Fig. 11d, in the distribution of the 24-h increment of relative vorticity for the composite of the 19 extremely

cold and dry TPV genesis events, the negative relative vorticity center is located over the northeast of the Kunlun Mountains, while the center of the positive 24-h increment of relative vorticity is located over the southeast, thereby creating a suitable background for TPV genesis and development.

It becomes clear that even under extreme cold and dry conditions, TPVs can also be generated over the northwestern TP under a favorable dynamic background, while an upstream anomalous westerly flow and a low geopotential system can bring positive vorticity to sustain the local shear line. The impinging westerlies on the Kunlun Mountains can trigger TPV genesis over its southeastern region due to the impact of surface friction.

6 Discussion and conclusions

In this study, we discussed the diversity of TPV genesis based on the $\Delta_{24h}\theta_e$ index. By using percentile analysis, the basic environments for June TPV genesis were grouped into two types, namely colder and drier, as well as warmer and moister. The initiation mechanisms for the two corresponding extreme categories, i.e., the first and last fifth percentiles, were investigated using a composite procedure from the perspective of PV generation. The main conclusions are summarized as follows:

1. *Characteristics of TPV genesis classified based on the $\Delta_{24h}\theta_e$ index.* A total of 374 June TPV genesis cases between 1980 and 2016 can be classified into two types according to the sign of the 24-h increment of equivalent potential temperature ($\Delta_{24h}\theta_e$) at the TPV genesis time, i.e., the negative type corresponding to colder and drier environments, and the positive type corresponding to warmer and moister environments. In terms of occurrence frequency, 70% of June TPVs are generated with a positive $\Delta_{24h}\theta_e$ index. After standardization, the numbers of the two types tends to be even. When the TPV cases are selected based on the the 5% and 95% percentiles of the standardized $\Delta_{24h}\theta_e$ index, all selected cases occurs in the western TP. The majority of TPVs with a positive standardized $\Delta_{24h}\theta_e$ index occur at night, whereas half of those with a negative standardized $\Delta_{24h}\theta_e$ index occur during the day. Overall, the results from diagnoses indicate that the $\Delta_{24h}\theta_e$ index can be used for identifying different environments at the TPV genesis time.
2. *TPV genesis mechanisms of the positive type from the PV perspective.* According to Eq. (1), PV generation is dominated by dynamic and thermodynamic processes. We demonstrate that for the positive type of TPV genesis, diabatic heating associated with moist processes dominates the TPV genesis when the local environment becomes warmer and moister (Fig. 3a). Composite anal-

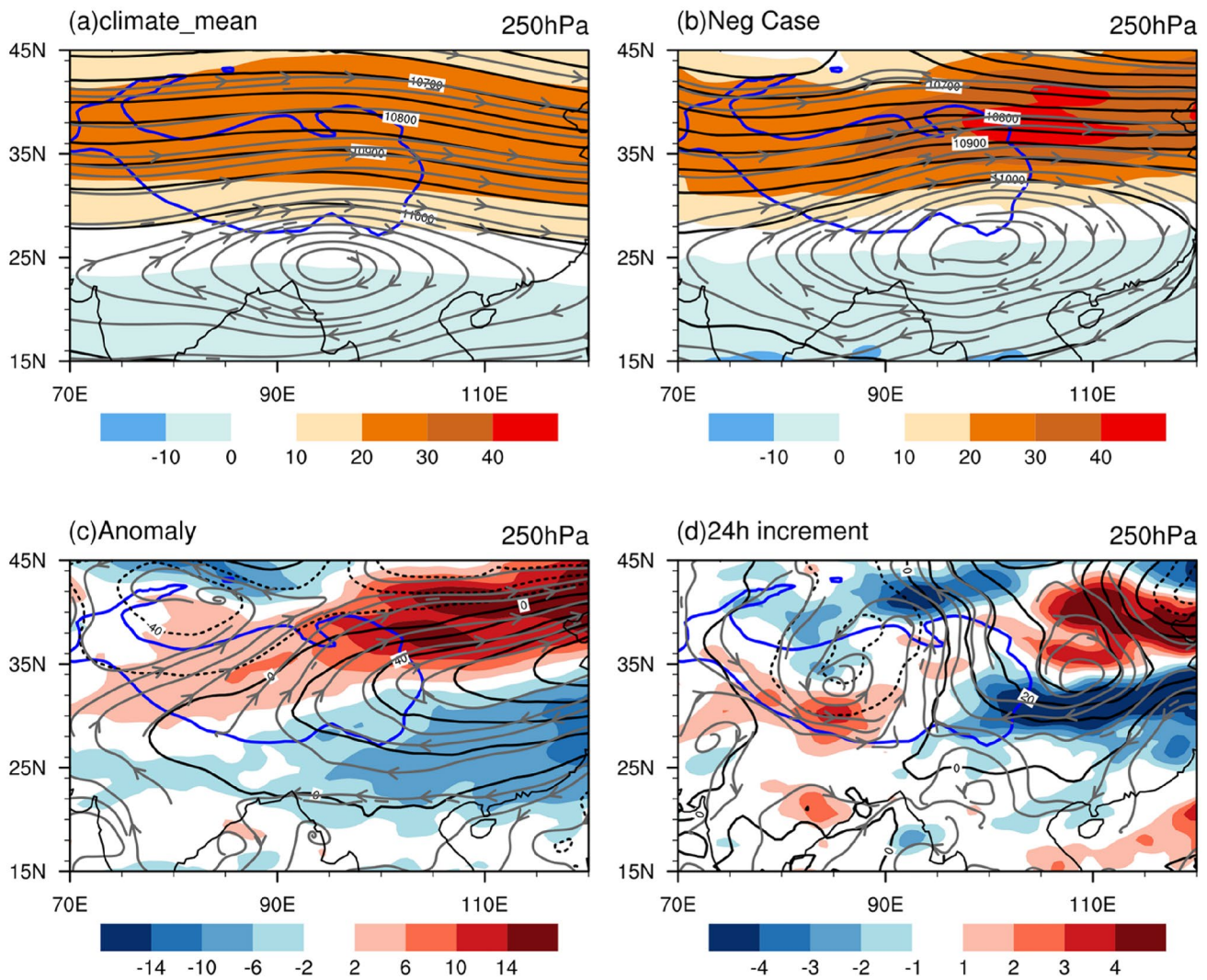


Fig. 10 Distributions at 250 hPa of the zonal wind speed (shading; unit: m s^{-1}), geopotential height (contours; unit: gpm), and streamlines for the **a** June climatology during 1980–2016, **b** composite of the 5% most negative index cases, and **c** anomalies (i.e., panel

b minus panel **a**). **d** Composite of the 24-h increment for the 5% extreme negative index cases. Dashed contour lines in panels **c**, **d** denote negative values. The solid blue contour lines in all panels indicate the TP boundary at 3000 m

ysis of circulation indicates that an obvious “negative on the west and positive on the east” dipole mode of geopotential height exists over the TP, thereby resulting in enhanced southerly flow across the southern boundary of the TP at 500 hPa (Fig. 4a) and easterly flow anomaly around the southern boundary of the TP at 700 hPa (figure not shown). With reinforced ascending airflow, anomalous easterlies transport water vapor to the western TP, resulting in increased sub-cloud entropy. The center of the prominent diabatic heat is associated with moist processes at 350 hPa, thereby leading to increasing diabatic heating with height (Fig. 6a). A local positive PV is generated, thereby favoring TPV genesis.

3. *Negative-type TPV genesis mechanisms—impact of friction.* For negative standardized $\Delta_{24h}\theta_e$ index cases, the

dynamical effects of large-scale circulation are more important. A prominent westerly flow prevails over the TP, both in the upper troposphere (Fig. 10b) and near the TP surface (Fig. 11a). In the upper troposphere, an anomalous trough develops over the northwestern TP, while an abnormal positive geopotential height dominates the area from the southeastern TP to eastern China, with west-southwesterly flow intensified over the western TP (Fig. 10c). The composite 24-h increment of geopotential height at the TPV genesis time presents a dipole pattern over the TP, with negative values on its west and positive on its east (Fig. 10d). Consequently, westerlies increase over the southwestern TP, whereas easterlies increase over the northwestern TP, thereby forming a zonally oriented shear line over the west-

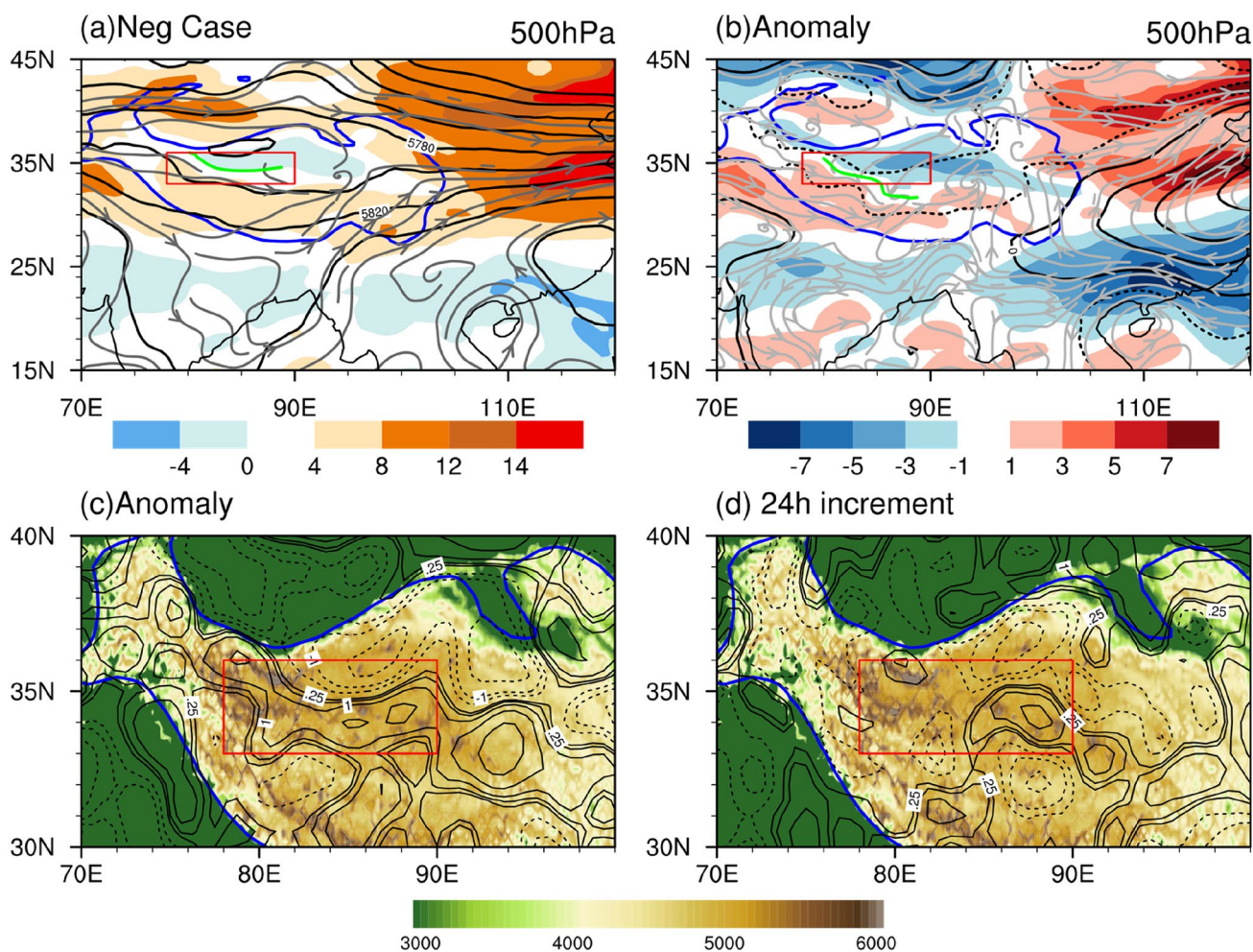


Fig. 11 Distribution at 500 hPa of the zonal wind speed (shading; unit: m s^{-1}), geopotential height (contour; unit: gpm), and streamlines for **a** the composite of the 5% most negative index cases, and **b** the corresponding anomalies from the June climatology during 1980–2016. **c** Same as panel **b**, but for the streamlines and relative vorticity (contour; unit: 10^{-5} s^{-1}). **d** Composite of the 24-h increment

of streamlines and relative vorticity (contour; unit: 10^{-5} s^{-1}) for the 5% extreme negative index cases. The green curves in panels **a**, **b** indicate the zero contour between 80° and 90° E . Dashed contours in panels **c**, **d** denote negative values. The solid blue contour lines in all panels indicate the TP boundary at 3000 m

ern TP. At 500 hPa, the negative geopotential height anomaly dominates over the entire TP, accompanied by cyclonic circulation (Fig. 11b). Anomalous westerlies develop over the southern TP, while easterlies develop over the north, thereby forming an anomalous zonal shear line near 35° N on the western TP, which is just south of the ridge of the Kunlun Mountains. Thus, the friction impact of the Kunlun Mountains on the impinging westerlies generates positive relative vorticity to the south and negative vorticity to the north (Fig. 11c). Mainly due to the zonal advection of vorticity, the centers of the negative and positive 24-h vorticity increment develop, over the northeast and southeast ends of the Kunlun Mountains, respectively. These conditions are conducive to TPV genesis and development over the

northwestern TP, even though the $\Delta_{24h}\theta_e$ index is negative.

This study explores the differences in genesis mechanisms between the two extreme categories of TPVs, which account for only 10% of the total TPV genesis cases. A preliminary investigation on universality based on the composite analysis of 60% cases, i.e., 30% for each positive and negative type, indicates that the critical circulation and thermal conditions elaborated in this study still present although with smaller magnitude (Figures not shown). Nevertheless, further studies are necessary to confirm the relationship between the environment and the “non-extreme” TPV genesis. Besides, the characteristics of those other types of TPV genesis remain unclear and require further investigations. Even for

these two extreme types of TPVs, how they evolve after genesis and what are the differences in their life history, migration direction and speed, and effects on downstream weather systems need to be further elucidated.

Acknowledgements The authors are in debt to Dr. Lin Zhiqiang for his efforts in making the TPV database available.

Author contributions All authors contributed to the study conception and design. Material preparation, and data collection were performed by YT. The methodology was proposed by GW and YT. Formal analysis was performed by YT, GW and BH. The first draft of the manuscript was written by YT and all authors commented on previous versions of the manuscript. All authors read and approved the final manuscript.

Funding This work was jointly supported by the National Natural Science Foundation of China (Grants 42288101, 42122035, 91937302, and 41730963), the Guangdong Major Project of Basic and Applied Basic Research (2020B0301030004) and the Strategic Priority Research Program of the Chinese Academy of Sciences (Grant XDB40030200).

Data availability The MERRA-2 reanalysis dataset is available at <https://disc.gsfc.nasa.gov/datasets?project=MERRA-2>. The TPV dataset is available at <https://www.sciencedb.cn/dataSet/handle/556>.

Declarations

Conflict of interest On behalf of all the authors, the corresponding author states that there is no conflict of interest.

Open Access This article is licensed under a Creative Commons Attribution 4.0 International License, which permits use, sharing, adaptation, distribution and reproduction in any medium or format, as long as you give appropriate credit to the original author(s) and the source, provide a link to the Creative Commons licence, and indicate if changes were made. The images or other third party material in this article are included in the article's Creative Commons licence, unless indicated otherwise in a credit line to the material. If material is not included in the article's Creative Commons licence and your intended use is not permitted by statutory regulation or exceeds the permitted use, you will need to obtain permission directly from the copyright holder. To view a copy of this licence, visit <http://creativecommons.org/licenses/by/4.0/>.

References

- Chen G, Sha W, Iwasaki T, Wen Z (2017) Diurnal cycle of a heavy rainfall corridor over East Asia. *Mon Weather Rev* 145(8):3365–3389. <https://doi.org/10.1175/MWR-D-16-0423.1>
- Curio J, Schiemann R, Hodges KI, Turner AG (2019) Climatology of Tibetan Plateau vortices in reanalysis data and a high-resolution global climate model. *J Clim* 32(6):1933–1950. <https://doi.org/10.1175/jcli-d-18-0021.1>
- Deng Z, Ge X, Yao X, Chen M (2022) Simulation study on the radiation impacts on the formation and development of a Tibetan Plateau vortex. *Chin J Atmos Sci* 46(3):541–556. <https://doi.org/10.3878/j.issn.1006-9895.2105.20215>
- Emanuel K, Neelin J, Bretherton C (1994) On large-scale circulations in convecting atmospheres. *Q J R Meteorol Soc* 120(519):1111–1143. <https://doi.org/10.1002/qj.49712051902>
- Ertel H (1942) Ein neuer hydrodynamische wirbelsatz. *Meteorologische Zeitschrift Braunschweig* 59:33–49
- Feng X, Liu C, Rasmussen R, Fan G (2014) A 10-yr climatology of Tibetan Plateau vortices with NCEP climate forecast system reanalysis. *J Appl Meteorol Climatol* 53(1):34–46. <https://doi.org/10.1175/jamc-d-13-014.1>
- Fu S, Tang H, Sun J, Zhao T, Li W (2022) Historical rankings and vortices' activities of the extreme Mei-yu seasons: contrast 2020 to previous Mei-yu seasons. *Geophys Res Lett*. <https://doi.org/10.1029/2021gl096590>
- Gelaro R, Mccarty W, Suárez MJ, Todling R, Zhao B (2017) The modern-era retrospective analysis for research and applications, version 2 (MERRA-2). *J Clim* 30(14):5419–5454. <https://doi.org/10.1175/JCLI-D-16-0758.1>
- Hoskins B, McIntyre M, Robertson A (1985) On the use and significance of isentropic potential vorticity maps. *Q J R Meteorol Soc* 111:877–946
- Lhasa Workgroup for Tibetan Plateau Meteorology Research (1981) Research of 500 hPa vortices and shear lines over the Tibetan Plateau in summer. Science Press, Beijing
- Li L, Zhang R (2021) Effect of upper-level air temperature changes over the Tibetan Plateau on the genesis frequency of Tibetan Plateau vortices at interannual timescales. *Clim Dyn* 57(1):341–352. <https://doi.org/10.1007/s00382-021-05715-x>
- Li L, Zhang R, Wen M (2011) Diagnostic analysis of the evolution mechanism for a vortex over the Tibetan Plateau in June 2008. *Adv Atmos Sci* 28(4):797–808. <https://doi.org/10.1007/s00376-010-0027-y>
- Li L, Zhang R, Wen M (2014a) Diurnal variation in the occurrence frequency of the Tibetan Plateau vortices. *Meteorol Atmos Phys* 125(3–4):135–144. <https://doi.org/10.1007/s00703-014-0325-5>
- Li L, Zhang R, Wen M, Liu L (2014b) Effect of the atmospheric heat source on the development and eastward movement of the Tibetan Plateau vortices. *Tellus A Dyn Meteorol Oceanogr* 66:1. <https://doi.org/10.3402/tellusa.v66.24451>
- Li L, Zhang R, Wen M (2018) Diurnal variation in the intensity of nascent Tibetan Plateau vortices. *Q J R Meteorol Soc* 144(717):2524–2536. <https://doi.org/10.1002/qj.3343>
- Li L, Zhang R, Wu P, Wen M, Duan J (2020a) Roles of Tibetan Plateau vortices in the heavy rainfall over southwestern China in early July 2018. *Atmos Res*. <https://doi.org/10.1016/j.atmosres.2020.105059>
- Li L, Zhu C, Zhang R, Liu B (2020b) Roles of the Tibetan Plateau vortices in the record Meiyu rainfall in 2020b. *Atmos Sci Lett*. <https://doi.org/10.1002/asl.1017>
- Lin Z, Zhou Z, Jia L (2013) Objective identifying method of Qinghai-Xizang Plateau vortex using NCEP/NCAR reanalysis dataset. *Plateau Meteorol* 32(6):1580–1588
- Lin Z, Guo W, Jia L, Yao X, Zhou Z (2020) Climatology of Tibetan Plateau vortices derived from multiple reanalysis datasets. *Clim Dyn* 55(7–8):2237–2252. <https://doi.org/10.1007/s00382-020-05380-6>
- Lin Z, Guo W, Yao X, Du J, Li W et al (2021) Tibetan Plateau vortex-associated precipitation and its link with the Tibetan Plateau heating anomaly. *Int J Climatol* 41(14):6300–6313. <https://doi.org/10.1002/joc.7195>
- Luo S, Yang Y (1992) A case study on numerical simulation of summer vortex over Qinghai-Xizang (Tibetan) Plateau. *Plateau Meteorol* 11:39–48
- Luo S, Yang Y, Lu S (1991) Diagnostic analyses of a summer vortex over Qinghai-Xizang Plateau for 29–30 June 1979. *Plateau Meteorol* 10:1–11
- Ma T, Liu Y, Wu G, Mao J, Zhang G (2020) Potential vorticity diagnosis on the formation, development and eastward movement of a Tibetan Plateau Vortex and its influence on the downstream precipitation. *Chin J Atmos Sci* 44(3):20–34
- Ma T, Wu G, Liu Y, Mao J (2022) Abnormal warm sea-surface temperature in the Indian Ocean, active potential vorticity over the Tibetan Plateau, and severe flooding along the Yangtze River in

- summer 2020. *Q J R Meteorol Soc* 148(743):1001–1019. <https://doi.org/10.1002/qj.4243>
- Qian Z, Shan F, Lv J, Cai Y, Chen Y (1984) Statistics of Qinghai-Tibet Plateau Vortices during the summer of 1979 and a discussion on the climatic factors of TPV genesis. Collection of the Tibetan Plateau meteorology experiments II. China Science Press, Beijing, pp 279–290
- Shen R, Reiter E, Bresch J (1986) Some aspects of the effects of sensible heating on the development of summer weather system over the Qinghai-Xizang Plateau. *J Atmos Sci* 43:2241–2260
- Thorpe A, Volkert H, Heimann D (1993) Potential vorticity of flow along the Alps. *J Atmos Sci* 50(11):1573–1590
- Tian S, Duan A, Wang Z, Gong Y (2015) Interaction of surface heating, the Tibetan Plateau vortex, and a convective system: a case study. *Chin J Atmos Sci* 39(1):125–136
- Wang B (1987) The development mechanism for Tibetan Plateau warm vortices. *J Atmos Sci* 44:2978–2994
- Wang X, Li Y, Yu S, Jiang X (2009) Statistical study on the Plateau low vortex activities. *Plateau Meteorol* 28(1):64–71
- Wu D, Zhang F, Wang C (2018) Impacts of diabatic heating on the genesis and development of an inner Tibetan Plateau Vortex. *J Geophys Res Atmos* 123(20):11691–611704. <https://doi.org/10.1029/2018jd029240>
- Wu G, Tang Y, He B, Liu Y, Mao J et al (2022) Potential vorticity perspective of the genesis of a Tibetan Plateau vortex in June 2016. *Clim Dyn* 58(11–12):3351–3367. <https://doi.org/10.1007/s00382-021-06102-2>
- Ye D, Gao Y (1979) The Tibetan Plateau meteorology. China Science Press, Beijing
- Ye D, Dao S, Li M (1958) The abrupt change of circulation over northern hemisphere during June and October. *Acta Meteorol Sin* 29(4):249–263
- Zhang FM, Wang CH, Pu ZX (2019) Genesis of Tibetan Plateau Vortex: roles of surface diabatic and atmospheric condensational latent heating. *J Appl Meteorol Clim* 58:2633–2651. <https://doi.org/10.1175/jamc-d-19-0103.1>
- Zhang G, Mao J, Liu Y, Wu G (2021) PV perspective of impacts on downstream extreme rainfall event of a Tibetan Plateau vortex collaborating with a Southwest China vortex. *Adv Atmos Sci* 38(11):1835–1851. <https://doi.org/10.1007/s00376-021-1027-9>
- Zhao Y, Chen D, Deng Y, Son S-W, Wang X et al (2021) How were the eastward-moving heavy rainfall events from the Tibetan Plateau to the lower reaches of the Yangtze River enhanced? *J Clim* 34(2):607–620. <https://doi.org/10.1175/jcli-d-20-0226.1>

Publisher's Note Springer Nature remains neutral with regard to jurisdictional claims in published maps and institutional affiliations.